



# Dominant modes of winter precipitation variability over Central Southwest Asia and inter-decadal change in the ENSO teleconnection

Sapna Rana<sup>1</sup> · James McGregor<sup>1</sup> · James Renwick<sup>1</sup>

Received: 11 September 2018 / Accepted: 2 July 2019 / Published online: 4 July 2019  
© Springer-Verlag GmbH Germany, part of Springer Nature 2019

## Abstract

This study contributes to an improved understanding of Central Southwest Asia (CSWA) wintertime (November–April) precipitation by analyzing the dominant spatial–temporal modes of the regional winter precipitation and examining their relationship with global sea surface temperature (SST) and large-scale atmospheric circulation fields, for 1950/51–2014/15. Empirical orthogonal function (EOF) analysis results show that the first mode (EOF-1) of winter precipitation is characterized by a mono-sign pattern, with significant links to El Niño–Southern Oscillation (ENSO). EOF-2 displays a north–south dipole related to the latitudinal shift in the jet stream position, while the west–east dipole in EOF-3 appears to be influenced by the thermal contrast between the equatorial regions and higher latitudes. Further, we focus on the interdecadal change of connection between wintertime ENSO and EOF-1 observed around the early 1980s. The relationship is weak during 1950/51–1983/84 (P1), but strong and statistically significant in 1984/85–2014/15 (P2). In P1, without the ENSO signal, EOF-1 related atmospheric circulation anomalies are confined mainly over the mid- to high-latitudes of the Northern Hemisphere, associated with the extratropical East Atlantic–Western Russia (EA–WR) teleconnection. In P2, however, a close connection to the tropical Pacific is observed that includes a pronounced SST expression similar to that of ENSO. As a result of the increased relationship between ENSO and EOF-1 in P2, the regional impact of EA–WR observed over CSWA in P1 is linearly superimposed by the anomalous hemispheric–wide atmospheric response forced by the ENSO conditions in the Pacific.

**Keywords** Central Southwest Asia · Winter precipitation · Atmospheric circulations · Inter-decadal change · ENSO

## 1 Introduction

Central southwest Asia (CSWA), defined here as the domain bounded by 20°–47°N, 40°–85°E is a semiarid and a water-scarce region (Oki and Kanae 2006) prone to large interannual and inter-decadal precipitation variations (Hoell et al. 2015a). Dominated by high mountain ranges from west to east—the Alborz, Zagros, Hindu Kush, Pamirs, Karakoram and the Himalayas (Fig. 1a), the complex orography of CSWA strongly modulates the weather systems and profoundly controls the regional distribution of precipitation (Barlow et al. 2005; Barlow and Tippett 2008; Rana et al. 2017). A large part of CSWA, which includes the western and the northern flanks of the domain, is beyond the usual

reach of the Indian monsoon [e.g., Fig. 2 in Rana et al. (2015)] with little precipitation during the warm summer season.

For much of CSWA, precipitation primarily occurs during the winter and early spring season of November–April [(NDJFMA); see Fig. 1c] when the region is within the subtropical belt of the upper-tropospheric westerly jet stream (Krishnamurti 1961). The intensification and southward excursions of the subtropical westerly jet bring moisture-bearing midlatitude synoptic storms into CSWA. As they traverse eastwards, they pass through a dense upper-air observing array over Europe, the Middle East, the Black Sea and the Caspian Sea regions (Schär et al. 2004). The moisture advection associated with these storms is typically from the west, including the Atlantic, the Mediterranean Sea, the Red Sea, the Persian Gulf, the Caspian Sea and the Arabian Sea (Barlow et al. 2005; Kar and Rana 2014). While propagating from west to east, the moisture-laden winds modify the regional circulations as they encounter the

✉ Sapna Rana  
sapna.rana@vuw.ac.nz

<sup>1</sup> School of Geography, Environment and Earth Sciences,  
Victoria University of Wellington, Wellington, New Zealand

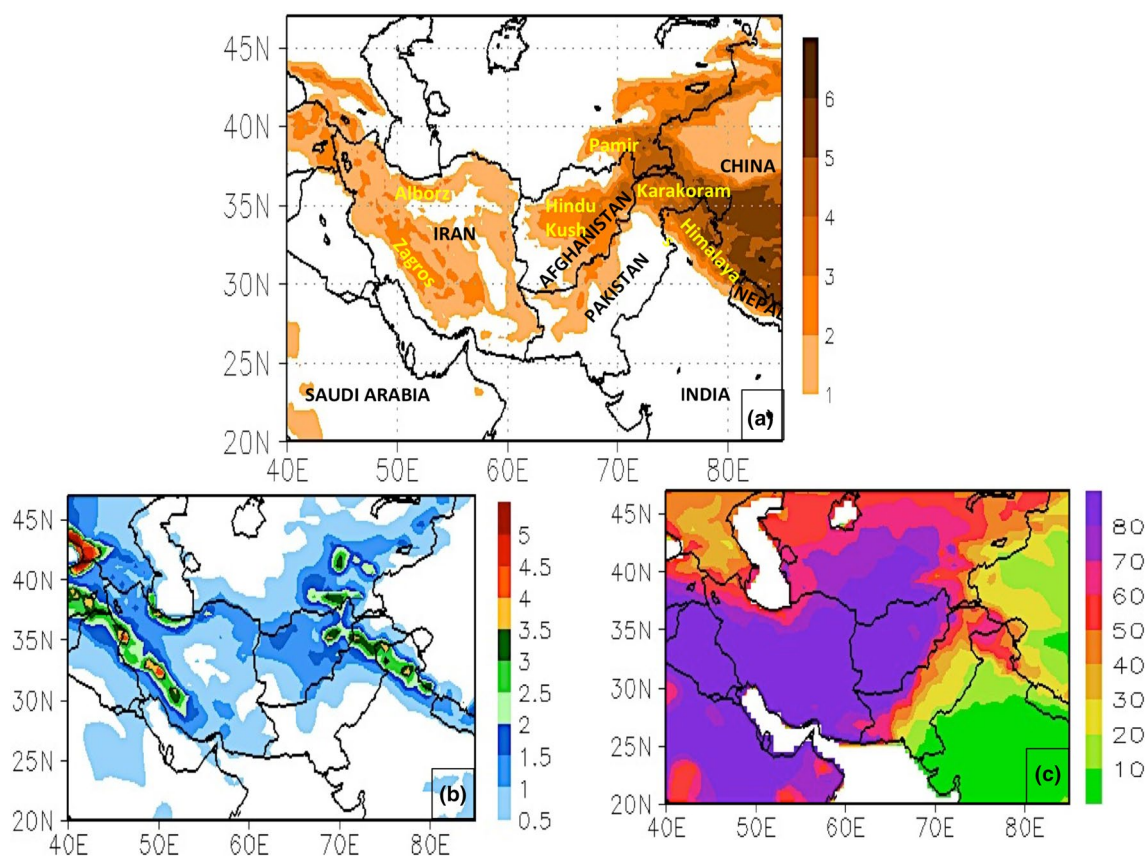


**Fig. 1** **a** Topography (km) of CSWA (20°–47°N, 40°–85°E), **b** spatial distribution of winter season precipitation (mm/day), and **c** percentage contribution of NDJFMA precipitation to the total annual precipitation over CSWA for 1950/51–2014/15

high mountain ranges of CSWA and generate precipitation via upslope lifting (Cannon et al. 2016; Barlow et al. 2016). The precipitation is mostly in the form of snow over the high mountain ranges, which accumulates as a seasonal snowpack throughout the cold months. The melting of this snow is an important source of water during the spring–summer season, which happens to coincide with the time of year when the regional water demand is highest. In addition to snow, winter rainfall in the sub-mountainous and low elevation areas is crucial for the widespread subsistence agriculture, industrial needs, and livelihood.

CSWA winter precipitation is strongly influenced by several large-scale modes of climate variability such as the El Niño–Southern Oscillation (ENSO), Pacific decadal oscillation (PDO), North Atlantic Oscillation (NAO), East Atlantic–Western Russia (EA–WR) pattern, Polar/Eurasian Pattern (PE), Indian Ocean Dipole (IOD) and others [for more details see Barlow et al. (2016)] at time scales ranging from sub-seasonal to seasonal and interannual to decadal (Barlow et al. 2005; Barlow and Tippett 2008; Hoell et al. 2012, 2013, 2015b; Kar and Rana 2014; Yin et al. 2014). A comprehensive review of boreal wintertime teleconnection studies highlights ENSO as an important driver of CSWA's

winter precipitation climate. Both observational and model analyses show that the two phases of ENSO, El Niño or La Niña, are related to statistically significant region-wide increases or decreases of winter precipitation (Mariotti 2007; Hoerling and Kumar 2003; Hoell and Funk 2013; Hoell et al. 2015a, 2017; Rana et al. 2017; 2018) by way of both baroclinic (Barlow et al. 2002; Hoell et al. 2012) and barotropic (Hoell et al. 2013; Shaman and Tziperman 2005) Rossby wave teleconnection mechanisms.

As evidenced by previous research ENSO-related precipitation modifications are substantial over CSWA. However, with the competing influence of various tropical and extratropical teleconnections on CSWA climate, the regional precipitation anomalies can be influenced by other concomitant non-ENSO modes of climate variability. These modes, depending on their relative strengths and phase combinations, tend to modify the seasonal precipitation either directly (during non-ENSO years) or by way of partly modulating the strength of the ENSO response (e.g. Yin et al. 2014; Barlow and Hoell 2015; Barlow et al. 2016; Liu et al. 2017; Rana et al. 2018). The above mechanisms are not mutually exclusive and a high degree of uncertainty remains in our understanding

of their individual role in CSWA's wintertime precipitation variability. Therefore, one of the motivations of this study is to statistically characterize the leading spatial and temporal patterns of CSWA wintertime precipitation variability using the conventional empirical orthogonal function (EOF) analysis (Wilks 2006) and examine the large-scale teleconnection links that govern the leading precipitation modes.

Furthermore, we focus on the leading mode [(EOF1) of CSWA winter precipitation] that explains a relatively large proportion of the region's precipitation variability and has a close relationship with tropical Pacific ENSO forcing as reported in Hoell et al. (2017). The authors also documented that the long-term relationship between wintertime ENSO (Niño-3.4) and CSWA precipitation varied in strength throughout the 20th century (1901–2012) and was strongest after the 1980s. Our recent study (Rana et al. 2018) also revealed that the influence of springtime Niño-3.4 (NAO) on CSWA winter precipitation strengthened to (weakened from) a statistically significant level around the early 1980s and continued to increase (decrease) thereafter. In particular, changes in ENSO characteristics including frequency, intensity, location, structure, and propagation during recent decades (Wang 1995; An and Wang 2000) have been shown to force stronger wintertime northern hemisphere circulations and significant precipitation modifications over CSWA (Hoell and Funk 2013; Hoell et al. 2014a, b) resulting in higher predictability and predictive skill of the regional precipitation after the 1980s period (Rana et al. 2018).

These studies suggest a possible inter-decadal change of connection between wintertime ENSO and CSWA precipitation around the early 1980s. Since it is unclear whether this relationship will remain strong in future, it is of interest to investigate how the connection between CSWA winter precipitation and the global atmospheric circulation changed in the context of the above discussion. We believe that addressing these issues will deepen our understanding of CSWA wintertime precipitation variability and may provide useful information for seasonal forecasting of the regional precipitation.

The rest of the paper is organized as follows. Section 2 describes the data and methods adopted in this study. Section 3 presents the spatial and temporal characteristics of the leading three (EOF-1, EOF-2, EOF-3) modes of winter (NDJFMA) precipitation variability over CSWA. The association between the three EOF modes of CSWA winter precipitation and the large-scale atmospheric circulations and global sea surface temperature (SST) anomalies are discussed in Sect. 4. Section 5 examines the inter-decadal change in ENSO–EOF-1 relationship and compares the circulations and SST anomalies before and after the inter-decadal change, followed by summary and discussion in Sect. 6.

## 2 Data and methods

### 2.1 Observed and reanalysis data

The present study employs two-monthly mean observed precipitation datasets over land. They are (1) the Global Precipitation Climatology Centre (GPCC) full data reanalysis version 7 (Schneider et al. 2014) available from <http://gpcc.dwd.de> for the period 1901–2013 and (2) the Climatic Research Unit (CRU) time series (TS) version 3.24.01 available from <https://crudata.uea.ac.uk/cru/data/> for the period 1901–2015 (Harris et al. 2014). The current analysis uses 0.5° latitude/longitude resolution for both GPCC and CRU data.

It is important to note that throughout the CSWA region, considerable uncertainty exists in the accuracy of gridded precipitation estimates (Barlow and Tippet 2008; Rana et al. 2015, 2017; Hoell et al. 2017). Some of the factors that contribute to this uncertainty are: sparse or non-existent precipitation observation network, political sensitivity, extreme topography, snow measurement errors and so on. In order to gain a better understanding of some of these issues, Rana et al. (2017) performed a comprehensive assessment of various precipitation datasets for CSWA and reported that in comparison to some of the currently available observational datasets (including CRU), GPCC precipitation estimates are qualitatively more realistic and reliable in this region. Therefore, the present study uses GPCC precipitation records from 1950 up to 2013 and the CRU dataset thereafter. The spatial maps of the CSWA wintertime precipitation climatology and its seasonal percentage contribution to the total annual precipitation for the analysis period (1950/51–2014/15) are shown in Fig. 1b, c, respectively.

Estimates of monthly mean observed SST (°C) data are drawn from the National Oceanic and Atmospheric Administration (NOAA) extended reconstructed SST version 5 (Huang et al. 2017; <http://www.esrl.noaa.gov/psd/data/gridded/>). This SST dataset is produced on a fixed 2° latitude–longitude resolution and is available from 1854 to the present. In this study, ENSO variability is represented by the Niño-3.4 index which is defined as the area averaged SST anomaly over the region 5°S–5°N, 170°–120°W.

Reanalysis atmospheric variables including monthly-mean sea level pressure (SLP), the geopotential height at 500-hPa (Z500) and 200-hPa (Z200), zonal and meridional components of winds at 700-hPa (U700; V700) and 200-hPa (U200; V200) are drawn from the National Centers for Environmental Prediction (NCEP)–National Center for Atmospheric Research (NCAR) at a fixed 2.5° × 2.5° latitude–longitude grid for 1948–2015.

## 2.2 Methods

EOF analysis is a widely used statistical technique to reduce the dimensionality of a complex data set into linear combinations of fewer new variables that represent the maximum possible fraction of the variance contained in the original data (Wilks 2006). Here, we use EOF analysis over CSWA (20°–47°N, 40°–85°E) by constructing an area-weighted covariance matrix of the observed winter precipitation for 1950/51–2014/15 period; and the first three patterns that explain nearly 45% of the total domain variance are analysed. Correlation and regression analyses are further applied to identify the physical mechanisms responsible for the connection between the three standardized EOF time series of CSWA precipitation with the wintertime global SST and large-scale atmospheric circulations. Statistical significance of the correlation coefficient at  $p < 0.10$  and  $p < 0.01$  is assessed using the two-sided Student's  $t$  test.

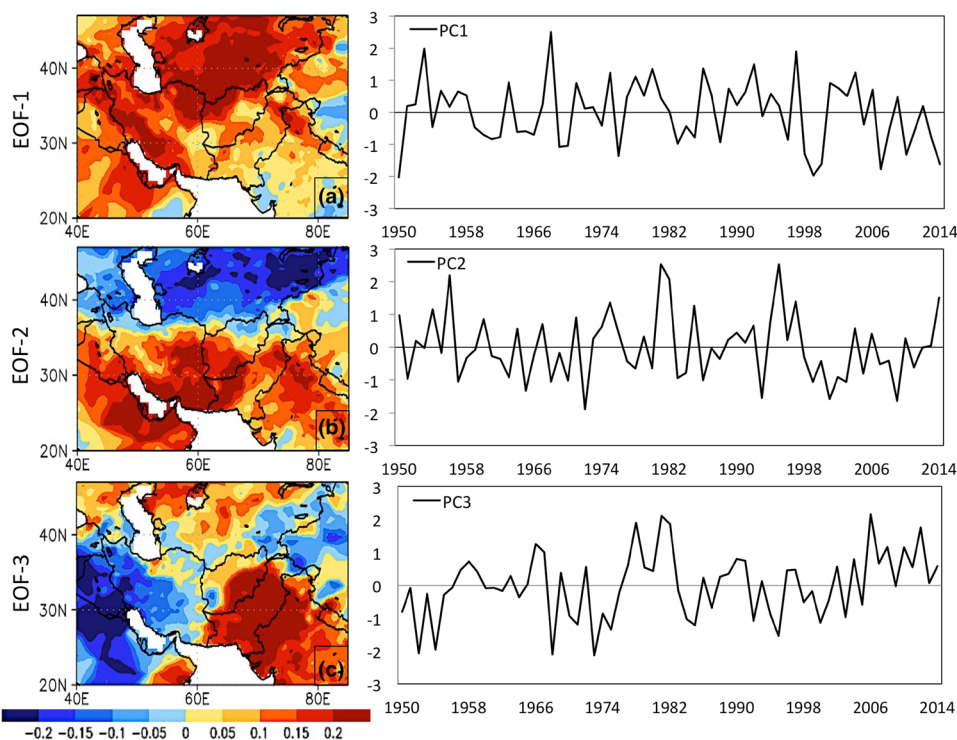
To document the inter-decadal change in the wintertime ENSO–CSWA precipitation relationship, we divide the entire analysis period (1950/51–2014/15) into two sub-periods: (1950/51–1983/84, P1) and (1984/85–2014/15, P2). The selection of the two subperiods is based on the 17-year sliding correlation of Niño-3.4 index with the leading (EOF-1) time series of CSWA precipitation. The underlying mechanisms pre- and post- the inter-decadal change of the ENSO impact on CSWA winter precipitation climate are investigated.

## 3 Characteristics of leading three EOF modes of CSWA winter precipitation

We start by examining the wintertime precipitation climatology (Fig. 1b) and its percentage contribution (Fig. 1c) to the total annual precipitation over CSWA for 1950/51–2014/15. The climatological precipitation displayed in Fig. 1b closely follows the principal mountain ranges of the region, with heaviest amounts falling on the western slopes of the high mountains. Yearly precipitation can exceed 1 m in some areas of the high mountains of western Iran, the Hindu-Kush Karakoram, as well as along the southern (eastern) shores of the Caspian (Black) Sea (Barlow et al. 2005). Regionally, wintertime precipitation demonstrates a high degree of spatial coherence (Hoell et al. 2015a) and makes a dominant contribution ( $> 65\%$ ) to the annual precipitation totals as seen in Fig. 1c.

The spatial patterns of the first three EOF modes of CSWA winter precipitation and time series of the corresponding principal components (hereafter PC) are shown in Fig. 2. The first EOF mode (Fig. 2a) explains 19% of the total domain variance and is characterized by a mono-sign pattern, with positive loadings over much of the region. This spatial pattern reflects the coherent variability of winter precipitation over the entire domain, consistent with the findings of previous studies (Hoell et al. 2015a; Kar and Rana 2014). The positive (negative) fluctuations in the polarity and amplitude of EOF1 are indicative of region-wide wetter

**Fig. 2** The spatial patterns and their corresponding normalized PC time series for the **a** first (EOF-1: 19%), **b** second (EOF-2: 15%), and **c** third (EOF-3: 10%) EOF modes of CSWA wintertime (NDJFMA) precipitation for the period 1950/51–2014/15





(drier) winter conditions. The PC time series associated with this mode (Fig. 2b) is positively correlated with the seasonally averaged year-to-year winter precipitation over CSWA ( $r=0.93$ ) and with ENSO ( $r=0.49$ ), both statistically significant at the 99% confidence level. More detail on these linkages is provided in Sect. 4.

The second EOF (Fig. 2b) of winter precipitation, explaining 15% of the total variance, displays a meridional dipole structure with a negative center of action in the north and a positive one in the south. The zero line of the dipole pattern is confined close to the climatological position of the winter tropospheric jet that lies between 20°N and 35°N (Krishnamurti 1961), suggesting that the second EOF mode of winter precipitation is presumably related to the fluctuations in the latitudinal position/intensity of wintertime jets over CSWA. Strong links have been established between the NAO and the variability in the speed and mean position of the mid-latitude westerly jet stream during the boreal winter (Rogers 1997; Luo et al. 2007; Strong and Davis 2007; Woollings et al. 2010). For example, Luo et al. (2007) reported that the positive (negative) NAO phase is related to the poleward (equatorward) shift of the westerly jet from its climatological position in the northern Hemisphere. However, in our case the PC2 time series associated with the second EOF mode does not demonstrate a significant linkage to the wintertime (NDJFMA) NAO index. A possible reason for this could be that a combination of different concomitant climatic modes such as the East Atlantic pattern (EA), the Scandinavian pattern (SCA), the EA–WR pattern and atmospheric blocking events can modulate the geographical location and intensity of the NAO's centres of action from the classic locations, used to compute the conventional station-based NAO indices (Woollings et al. 2010; Moore and Renfrew 2012; Comas-Bru and McDermott 2013). Moreover, various regional circulation patterns and large-scale atmospheric processes including tropical and extratropical teleconnections (e.g. ENSO, EA–WR, PE and Siberian High) have been linked to changes in the westerly storm-tracks accompanied by shifts in wintertime jet stream flow pattern over the CSWA region (Yin et al. 2014; Barlow et al. 2016; Cohen et al. 2014; Lioubimtseva 2015; Wolff et al. 2017) either directly or by way of partly modulating the strength of the associated teleconnections (Rana et al. 2018). It may be for these reasons that the PC2 time-series is not strongly correlated with any particular mode. See Sect. 4 for more details.

The third EOF mode of CSWA winter precipitation (Fig. 2c) explains 10% of the total variability and mostly features a zonal dipole with opposite precipitation variations in the western and eastern parts of the region. Structurally, the pattern represents longitudinal variations in the mean structure and flow (ridges and troughs) of Rossby waves associated with the subtropical jet stream over CSWA. It has

been noted that the strength of the jet stream is influenced by the magnitude of the meridional temperature gradient between the equatorial regions and the higher latitudes, such that the reduction in the north–south temperature gradient slows down the jet-stream zonal velocity and increases its tendency to meander (Francis and Vavrus 2012; Hassanzadeh et al. 2014). A similar west–east precipitation dipole structure across CSWA has been reported in Hoell et al. (2017) and Rana et al. (2018), who used different statistical approaches to characterise the long-term precipitation variability over the CSWA region. The PC3 time series displaying the temporal component of this mode shows a period of moderate variability before the mid-1990s, followed by a mild upward trend and increased variability, likely associated with an increase in the frequency of dry conditions over CSWA linked to the rapid warming of the Indo-west Pacific and the Atlantic Ocean SSTs in the recent decades (Compo and Sardeshmukh 2010; Hoell and Funk 2014; McGregor et al. 2014).

## 4 Association with global SST and large-scale atmospheric circulation anomalies

To demonstrate the physical sense of the three leading EOF modes of CSWA winter precipitation and to verify their relationship with the large-scale patterns of climate variability; spatial maps of SST, SLP, geopotential height, zonal and meridional winds anomalies were obtained using regression of the corresponding fields onto PC1 (Fig. 3), PC2 (Fig. 4) and PC3 (Fig. 5) time series.

### 4.1 EOF-1 associated climate anomalies

In Fig. 3a, the SST anomaly pattern for PC1 shows strong and statistically significant positive SST anomalies in the central-eastern tropical Pacific accompanied by negative anomalies over the western Pacific sector. This pattern is spatially similar to the warm phase of the ENSO cycle; that has its origin in the tropical Pacific Ocean with teleconnections reaching far beyond the Pacific sector (Latif and Barnett 1995; Neelin et al. 1998). Consistent with the distribution of SST anomalies associated with PC1, the SLP map in Fig. 3b exhibits a large-scale seesaw pattern of statistically significant SLP anomalies in the tropical Indo-western Pacific and the eastern Pacific Ocean, characteristic of the negative phase of the Southern Oscillation. In the North Atlantic sector, the SST anomalies bear some resemblance to the negative phase of the NAO cycle, which is usually observed during El Niño winters (Gershunov and Barnett 1998; Graf and Zanchettin 2012) and has been linked with the formation and persistence of atmospheric blocking

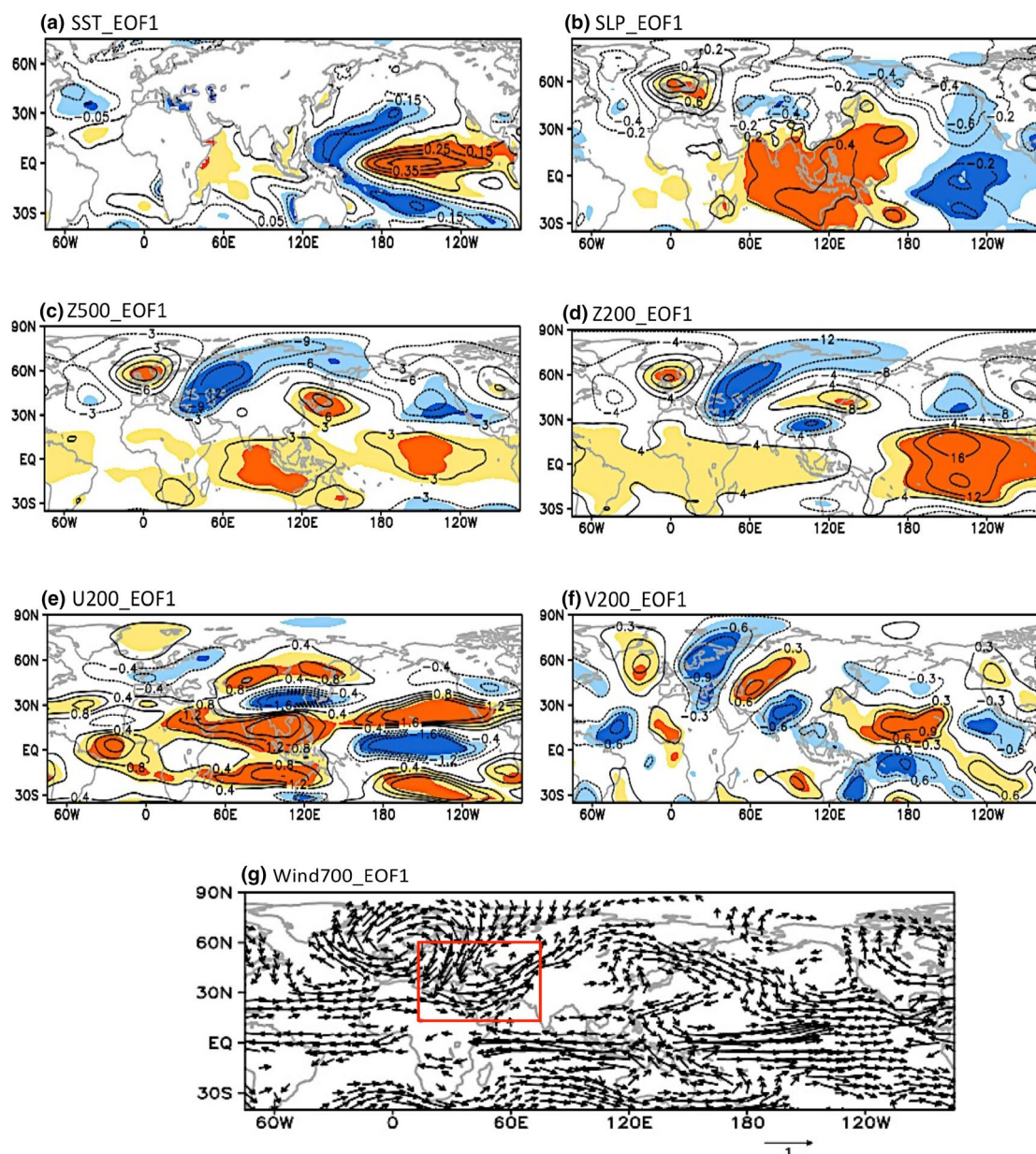


**Fig. 3** The regression maps of **a** SST, **b** SLP, **c** geopotential height at 500-hPa, **d** geopotential height at 200-hPa, **e** zonal wind at 200-hPa, **f** meridional wind at 200-hPa, and **g** wind vectors at 700-hPa onto PC1 time-series associated with EOF-1 for the period 1950/51–2014/15. Solid (dashed) contours denote positive (negative) values and zero

lines are omitted. The contour interval is 0.1 °C in **a**; 0.2 hPa in **b**; 3 m in **c**; 4 m in **d**; 0.4 m/s in **e** and 0.3 in **f**. The light and dark shadings in the figures (**a**–**f**) indicate that the correlation coefficients are significant at  $p < 0.10$  and  $p < 0.01$ , respectively

episodes in the North Atlantic sector (Shabbar et al. 2001). Supporting the above, a blocking-like dipole structure is evident in the SLP regression map (Fig. 3b) with a positive centre of action sitting over western Europe and a secondary centre of opposite sign over Greenland and further south, which is fairly similar to the blocking pattern described in Cassou et al. (2004).

Previous research has shown that the key system that bridges the ENSO-related variations in the Pacific Ocean and

CSWA's regional precipitation climate is through an eastward propagating Rossby wave train that emanates from the central equatorial Pacific Ocean and extends eastwards over North America, the Atlantic, and the Middle East into western Asia (Shaman and Tziperman 2005; Barlow and Tippet 2008). Large-scale equivalent barotropic Rossby waves propagate over the CSWA region (Hoell et al. 2013, 2015a; Rana et al. 2018) as evidenced by the statistically significant geopotential height anomalies of the same sign at Z500 hPa



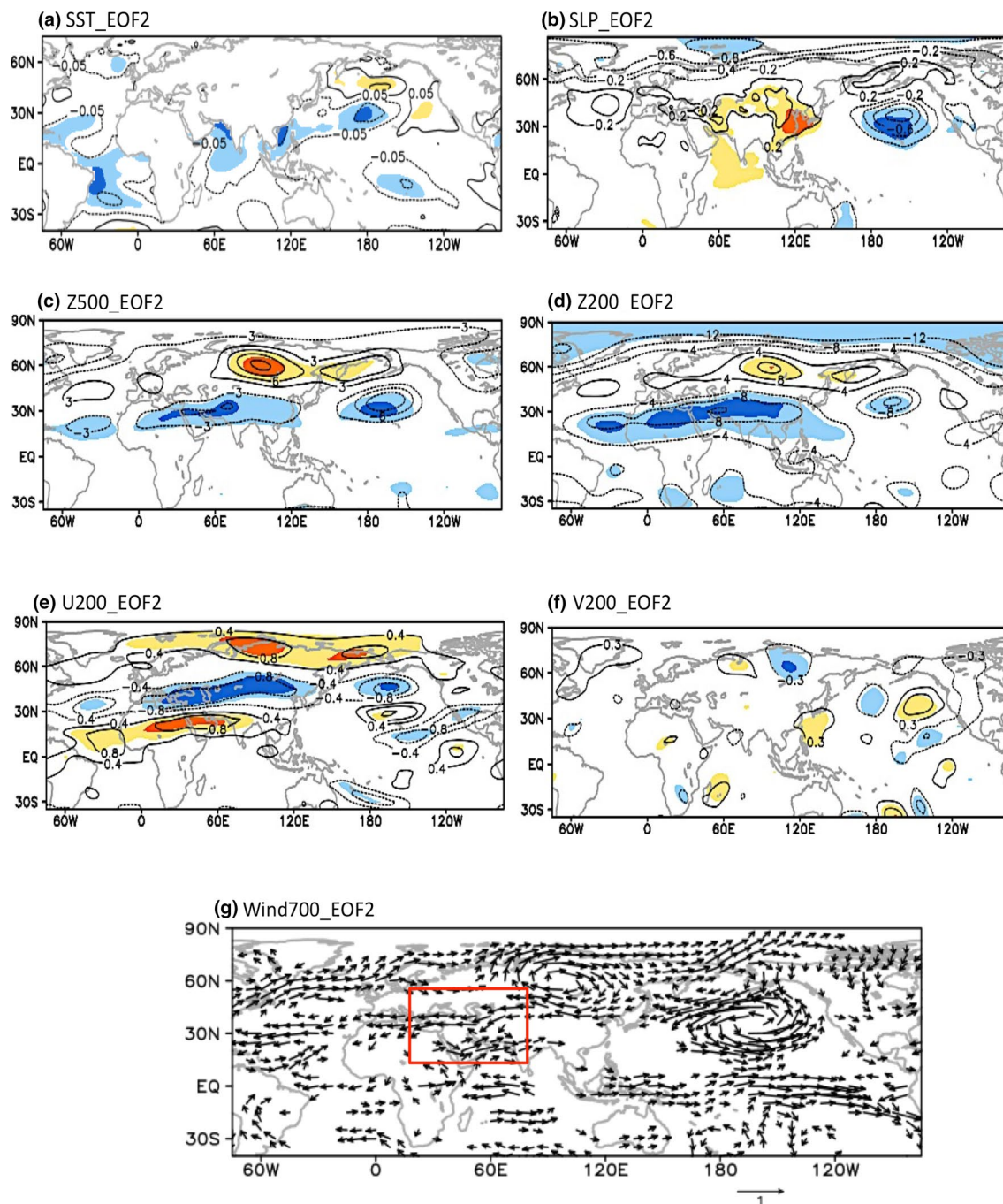


**Fig. 4** As in Fig. 3, but for PC2 time-series associated with EOF-2

and Z200 hPa in Fig. 3c, d, respectively. In addition to the stationary barotropic Rossby wave mechanism that impacts CSWA from the west, ENSO teleconnections also influence the regional climate of CSWA by the westward-propagating baroclinic Rossby waves (Barlow et al. 2002, 2007; Hoell et al. 2012) associated with the Gill–Matsuno-type circulation response (Matsuno 1966; Gill 1980). In Fig. 3, the tropically forced baroclinic response can be seen over India

and China (~30°N, 120°E) in the Z200 hPa and U200 hPa fields, but is somewhat overshadowed by the hemispheric-wide strong equivalent barotropic signal. These results show that anomalous warming in the equatorial eastern Pacific associated with El Niño induces an anomalously cold-core cyclonic trough (low pressure) over CSWA; that interacts with the mean mid- and upper-level tropospheric jet flows, resulting in a thermodynamically-forced warm temperature

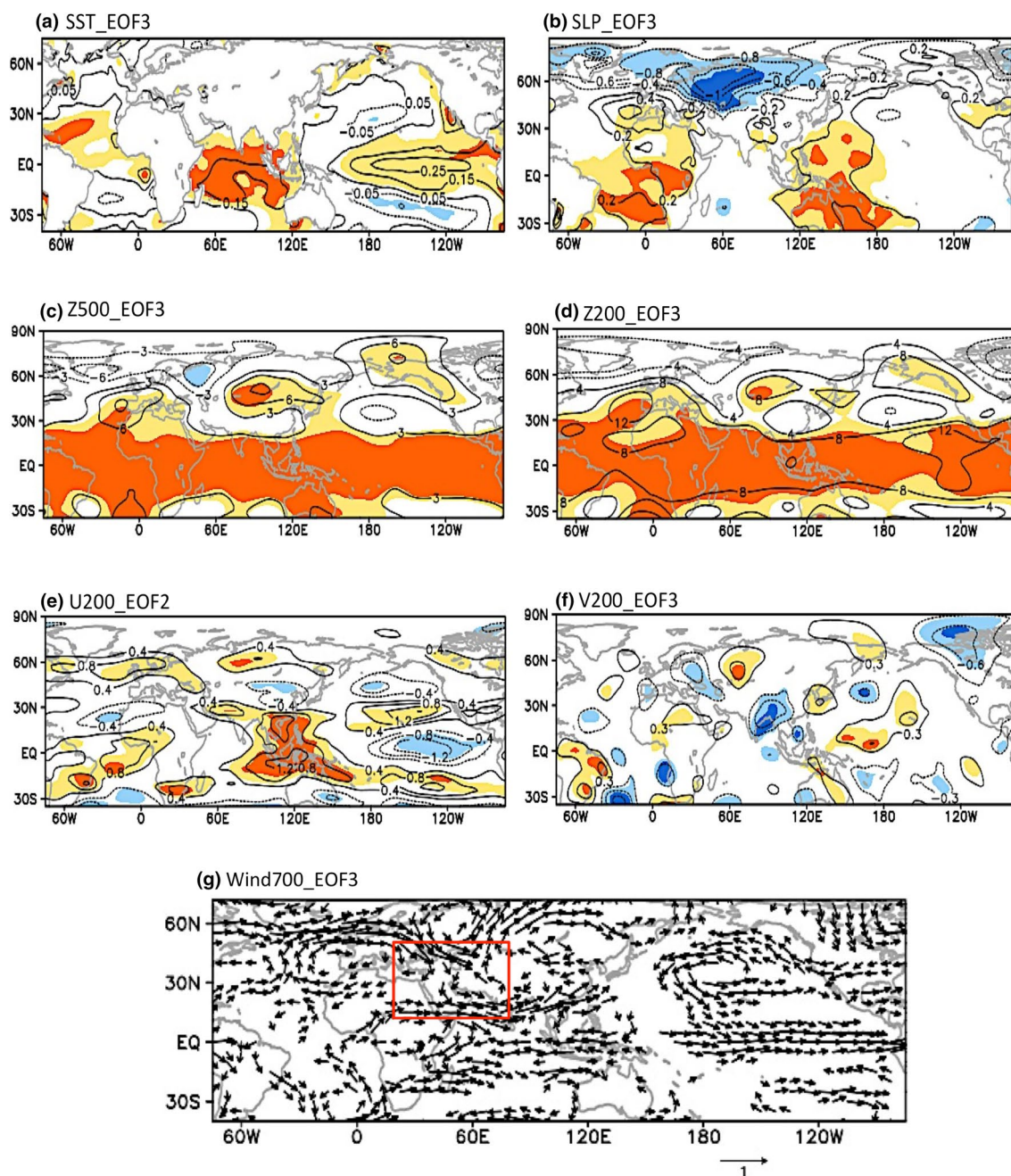


**Fig. 5** As in Fig. 3, but for PC3 time-series associated with EOF-3

advection and precipitation-enhancing anomalous ascent over CSWA that extends throughout the troposphere (Hoell et al. 2013, 2017). The reverse is true during La Niña years (Rana et al. 2018).

Correspondingly, the regression of the zonal wind component at 200-hPa (Fig. 3e) onto PC1 shows statistically significant negative anomalies (easterly flow anomalies) across the equatorial Pacific Ocean, indicative of a weaker-than-normal Walker Circulation in response to El Niño conditions. Another prominent feature is the zonally-elongated

band of positive (westerly) wind anomalies, circumnavigating the upper troposphere, and meridionally confined to latitudes ~25°–30° in the region of the subtropical westerly jet. Graf and Zanchettin (2012) showed that during warm ENSO events, in particular for central Pacific El Niños, the Rossby waves generated by anomalous atmospheric heating in equatorial latitudes may become meridionally trapped by the subtropical jet and propagate eastward within the jet waveguide causing perturbations over the Atlantic and European sector. In fact, the 200-hPa meridional wind anomalies shown in



Fig. 3f reflects a Rossby wave-like structure that appears to be originating from the equatorial Pacific (around the dateline) and propagating eastward as a series of cyclonic and anticyclonic features that are well observed over the Atlantic, Europe and western Asia. Furthermore, the significantly deepened trough as noted in the height anomalies appears as anomalous cyclonic circulation over CSWA at the lower 700-hPa level as shown in Fig. 3g. The circulation around this cyclonic center is associated with an enhanced southwesterly flow pattern across much of the CSWA region (within the red box in Fig. 3g), which advects moist air from the adjoining Arabian Sea and Indian Ocean basin, thereby increasing the regional winter precipitation during the warm ENSO phase.

## 4.2 EOF-2 associated climate anomalies

For the second EOF mode, the regression maps of SST (Fig. 4a) and SLP (Fig. 4b) onto PC2 show notably different sources of variability and associated atmospheric circulation structures, compared to those obtained for PC1. The SST anomalies are much weaker in magnitude with significance occurring only over limited areas of the three ocean basins. In the North Pacific sector, the SST pattern manifest features similar to the second mode of North Pacific SST variability, which is termed as the Victoria mode (Bond et al. 2003) or the North Pacific Gyre Oscillation (NPGO; Di Lorenzo et al. 2008). The corresponding atmospheric response to NPGO appears as a meridional pressure dipole between Alaska and Hawaii that has a strong resemblance to the North Pacific Oscillation (NPO) signature (e.g. Fig. 2 in Furtado et al. 2011; Linkin and Nigam 2008) and was first identified by Walker and Bliss (1932). Significant positive SLP anomalies also occur over a large part of East Asia with a spatial structure that represents a southward migration and a westward extension of the Siberian High from its climatological position of 40°–60°N, 80°–120°E. Based on the above it appears that the intensity and location of the Siberian High also plays a role in EOF-2 variability. Further, in the North Atlantic sector, the low-pressure anomalies over the Icelandic region and throughout the Arctic combined with high-pressure anomalies spanning the central latitudes of the North Atlantic between 35°N and 45°N represent a pressure dipole structure, reminiscent of NAO anomalies. Here, the most notable feature is that the atmospheric anomalies associated with PC2 are confined largely to the mid-to-high-latitudes of the Northern Hemisphere; implying that the tropical forcing plays a lesser role in the variability of the second EOF mode of CSWA winter precipitation, unlike the first EOF mode.

The regression map of Z500 (Fig. 4c) and Z200 (Fig. 4d) display a zonally oriented tripolar pattern of negative–positive–negative height anomalies extending

in the meridional direction over the Northern Hemisphere. Meanwhile, the height anomalies in the Pacific Ocean broadly resemble the western Pacific (WP) teleconnection pattern, which is the upper-air signature of the NPO variability in SLP (Linkin and Nigam 2008). The similar sign of height anomalies at 500-hPa and 200-hPa feature an equivalent barotropic vertical structure. The shape and the location of the twin statistically significant narrow bands of negative geopotential height anomalies (cyclones) located around 25°N and 60°N correspond to a slight equatorward and poleward shift in the position of the subtropical and polar front jet stream, respectively. The two jets are well separated from each other by a strong positive height anomaly centre located over central Russia and Mongolia associated with the Siberian anticyclone. These results are further supported by the 200-hPa zonal wind regression map (Fig. 4e) that exhibit a more prominent tripolar structure with zonally elongated and meridionally tighter zonal wind anomalies spanning the entire Northern Hemisphere. Statistically significant positive (westerlies) zonal wind anomalies are noted along the two jet axis, while the occurrence of negative (easterlies) wind anomalies at latitudes in between the jets suggest a weakening of the background westerlies in conjunction with the anticyclonic flow coming from the westward progression of the Siberian High over northern central Asia. The relationship between PC2 and the 200-hPa meridional wind component is rather weak or almost non-existent as seen in Fig. 4f. Hence the second mode of CSWA winter precipitation appears to be dominated by variations in the latitude and strength of the subtropical jet and zonal flow across Eurasia.

An interesting feature to note in the regressed wind anomalies at 700-hPa (Fig. 4g) is that the out-of-phase meridional dipole observed in the North Pacific SLP and geopotential height anomalies give rise to a dominant anticyclone–cyclone couplet that is associated with a strong easterly flow anomaly close to the nodal point (~48°N) and strengthens the prevailing easterlies of the Siberian anticyclone. Previous works have indicated the role of Siberian High in modifying the influence of the westerly storm systems over Northern Hemisphere mid-latitudes (Makorgianis et al. 1981; Hasanean et al. 2013; Panagiotopoulos et al. 2005; Cannon et al. 2014; Wolff et al. 2017). Consistent with the above findings, our results show that the westward extension of the Siberian anticyclone into central Asia and Europe, along with the northwestward nudging of the NPO/WP pattern contributes towards the maintenance of upper-level ridges over northern CSWA. This ridge blocks the eastward propagating westerly storm systems, restricting their flow to a more southerly track that results in more precipitation on the southern side of the CSWA region as shown in Fig. 2b.

### 4.3 EOF-3 associated climate anomalies

For the third EOF mode of CSWA winter precipitation, the SST regression map (Fig. 5a) associated with PC3 reveals three distinct tropic-wide areas of statistically significant positive SST anomalies. This pattern is fairly similar to the observed tropical SST trend noted for the last half century (e.g. Fig. 3a in Shin and Sardeshmukh 2011), the principal feature of which is the long-term warming of the Indian and the Pacific Ocean (Hoerling et al. 2001). The above result is consistent with the findings of Hoell et al. (2017), who reported that the west–east precipitation dipole pattern over CSWA (similar to the one depicted in Fig. 2c) is related to the warming of the Indian and Pacific Ocean SST. Also in Fig. 5b, the SLP response associated with PC3 depicts a strong midlatitude–tropical link, marked by a sharp tri-polar meridional pressure gradient with statistically significant negative pressure anomalies in the mid-to-high latitudes of the cold Eurasia/North Atlantic and two separate positive anomaly centres situated over the adjacent warm western Pacific/Australia and Africa/South Atlantic. Since the subtropical jet stream is a thermally driven phenomenon, a weaker (stronger) thermal contrast or SLP gradient tends to favour (inhibit) the north–south excursions, i.e. wave amplitude and waviness of the jet stream. In other words, an increased north–south meandering of the jet stream results in slower progression of weather systems and more frequent atmospheric blocking events that can lead to extreme weather events (Hassanzadeh et al. 2014; Barriopedro et al. 2006).

The above results provide reasonable evidence that the west–east precipitation pattern across CSWA (represented as EOF-3) is potentially related to the longitudinal changes in the zonal velocity of the westerly jet stream that occurs in proportion to the temperature/pressure changes forced by the meridional gradient of the diabatic heating. In response to the anomalous surface heating, the geopotential height anomalies at 500-hPa (Fig. 5c) and 200-hPa (Fig. 5d) associated with PC3 indicate a strong connection to the tropics with statistically significant positive height anomalies spanning the entire tropical region. Upstream of the Indian Ocean, an accompanying feature in the extratropical Northern Hemisphere is a less significant negative geopotential height anomaly pattern stretching from the North Atlantic to the Ural region, between positive anomalies positioned over the Mediterranean Sea and over southern Siberia. This tripolar pattern bears a close resemblance to the type 1 Eurasian pattern (Barnston and Livezey 1987), the Scandinavian pattern (Bueh and Nakamura 2007; Liu et al. 2014) or the Ural-Siberian blocking (Cheung et al. 2012). Here it is important to note that Liu et al. (2014) identified an important role of cold (warm) Indian Ocean SST anomalies in the formation and

maintenance of the positive (negative) Scandinavian pattern during the winter months.

In Fig. 5e, the regressed upper-tropospheric zonal wind anomalies associated with PC3 exhibit a weak westerly flow over North Africa and the Middle Eastern region. A zonally oriented band of positive (westerly) wind anomalies is observed at 60°N latitude that extends southeastwards over the Black Sea and the Caspian Sea region into CSWA. In the tropical and subtropical central Pacific, the zonal wind anomalies are similar to those related to the warm phase of ENSO. Meanwhile, the 200-hPa meridional wind component in Fig. 5f displays a prominent wave-like anomaly pattern with statistically significant centres of action encompassing much of the CSWA region. At the surface, the regressed wind fields (Fig. 5g) feature a cyclonic centre at 60°N–60°E, sandwiched between two large anticyclones that occupy most of the North Atlantic-European region in the west and central Siberia in the East. This pattern corresponds well to the extratropical positive–negative–positive anomaly centres of the Scandinavian pattern noted in the regressed height anomaly map in Fig. 5c. Here, the circulation response associated with the anticyclone over Europe and the cyclone over the Ural mountains generates a cold–dry northerly flow over the western flank of the CSWA region, resulting in negative precipitation loadings over western CSWA that are consistent with the see-saw pattern depicted in Fig. 2c. On the other hand, a strong westerly flow is observed along the southern flank (~10°N–20°N) of the CSWA region coming from Africa into the Arabian Sea, and extending up to central India and beyond. At the eastern periphery of the CSWA region (within the red box), the circulation pattern indicates a southerly flow into the eastern flanks of the CSWA region. This southerly flow from the Arabian Sea is associated with precipitation enhancing moist air advection into CSWA, consistent with the positive polarity of EOF loading pattern shown in Fig. 2c.

## 5 Inter-decadal change of connection between the wintertime ENSO and EOF-1

Here we focus on the inter-decadal change of the connection between ENSO and EOF-1 of CSWA winter precipitation variability. It has been established herein (Fig. 3) and previously (Hoell et al. 2017; Rana et al. 2018) that the leading mode of CSWA winter precipitation is closely related to the ENSO phenomenon. Using the Niño-3.4 index as an indicator of ENSO, Fig. 6a presents the interannual variability of the DJFMA averaged Niño-3.4 index and the normalized PC time series (i.e. PC1) associated with EOF-1 for the period 1950/51–2014/15. The year-to-year variations in the Niño-3.4 index and PC1 display both same-sign and opposite-sign changes during the analysis period. A close

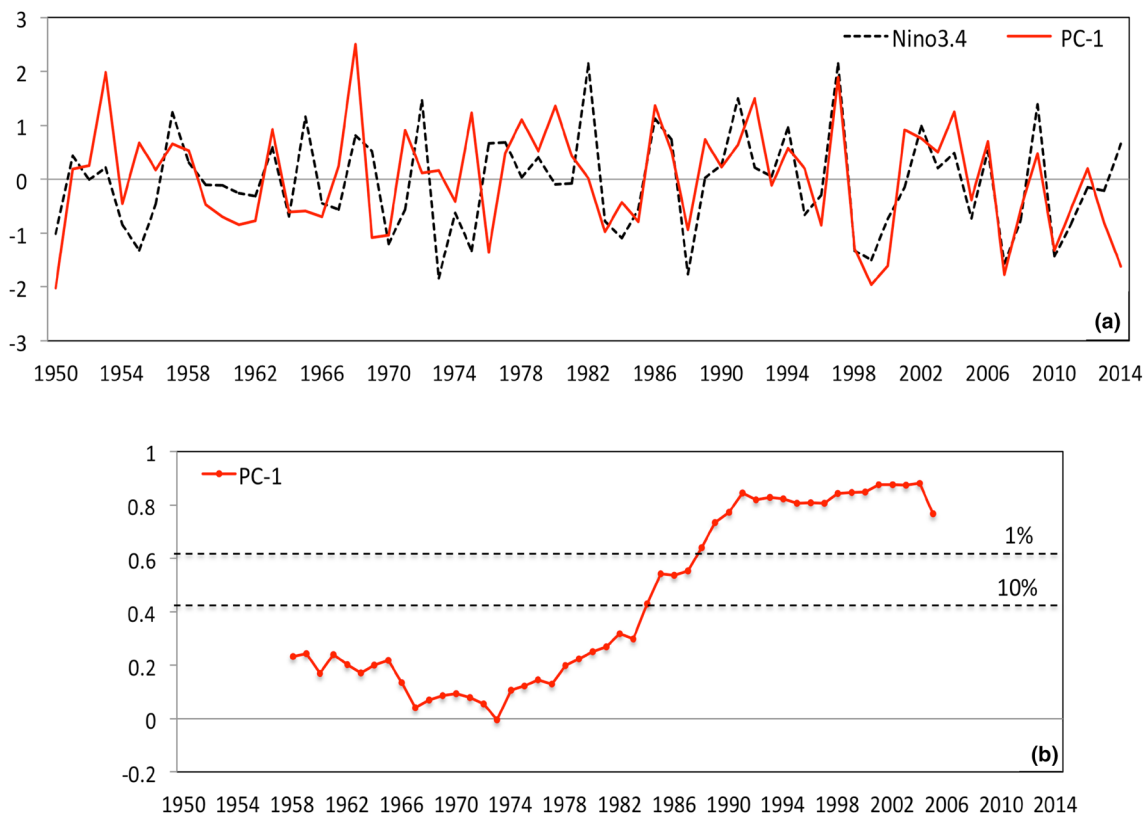


**Fig. 6** **a** Time series of the wintertime (NDJFMA) Niño-3.4 index and the normalized PC1 time-series associated with EOF-1 during 1950/51–2014/15. **b** Sliding correlations between Niño-3.4 index and

the PC1 time-series displayed at the central year of a 17-year window. The horizontal dotted lines in **b** indicates the correlation is significant at the 10% (0.41) and 1% (0.61) confidence level

examination shows that opposite-sign variations often occurred during the period from the 1950s through the early 1980s, while same-sign variations appear to dominate after the mid-1980s.

The sliding correlation between PC1 and the Niño-3.4 index with a 17-year window is shown in Fig. 6b. The impact of ENSO on EOF-1 variability is weak between 1950 and 1980, but strong and statistically significant after the mid-1980s. Many previous studies [e.g., Kumar et al. 1999; Van Oldenborgh and Burgers 2005; Lopez-Parages and Rodriguez-Fonseca 2012; Jia and Ge 2017] have found a non-stationary relationship between the surface climate and the ENSO teleconnections in different regions around the globe. These variations are often explained by changes in the background climate related to (1) the interdecadal variability of the midlatitude atmosphere (Gershunov and Barnett 1998; Diaz et al. 2001) (2) the influence of global warming (Stevenson 2012; Cai et al. 2015) (3) or by mere chance in which the low-frequency SST variations did not exert a modulating effect (Sterl et al. 2007). Since a similar change in the impact of ENSO teleconnection has been reported for CSWA (Hoell et al. 2017; Rana et al. 2018); therefore, in the following two separate sub-periods are discussed, with one

sub-period defined from 1950/51 to 1983/84 (P1) and the other from 1984/85 to 2014/15 (P2).

### 5.1 The EOF-1 associated global SST and large-scale atmospheric circulation anomalies in P1 and P2

Regression maps of SST and SLP onto PC1 time series associated with EOF-1 are examined for the two periods P1 and P2 and depicted in Fig. 7. During P1, the SST anomalies linearly correlated with EOF-1 are weak (Fig. 7a) while during P2 (Fig. 7b) there is a clear SST anomaly contrast between the warm central-eastern and cold western tropical Pacific Ocean, mimicking an El Niño-like structure. The regression map of SST (Fig. 7a) and SLP onto PC1 (Fig. 7c) shows that without the influence of ENSO, the atmospheric response anomalies in P1 are mainly constrained over the mid- to high-latitudes of the Northern Hemisphere; whereas a significant connection to the tropical Pacific is observed in P2 (Fig. 7d) indicating that ENSO has a closer and more persistent relationship with EOF-1 after the 1980s.

The EOF-1 related atmospheric circulations at the mid- and upper-tropospheric levels for the two sub-periods are depicted in Fig. 8. The 500- and 200-hPa regressed height



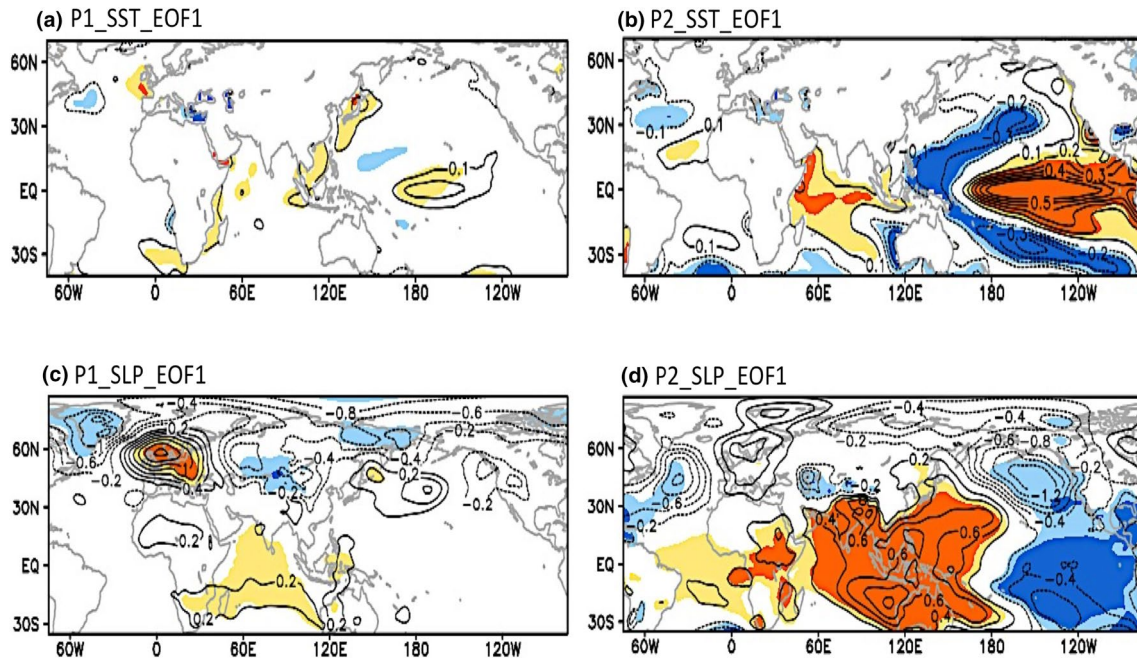


**Fig. 7** The regression maps of **a, b** SST and **c, d** SLP onto the PC1 time series associated with EOF-1 for P1 [1950/51–1983/84] (**a, c**) and P2 [1984/85–2014/15] (**b, d**). Solid (dashed) contours denote positive (negative) values and zero lines are omitted. The contour

interval is 0.1 °C in **a, b**; and 0.2 hPa in **c, d**. The light and dark shadings in the figures (**a–d**) indicate that the correlation coefficients are significant at  $p < 0.10$  and  $p < 0.01$ , respectively

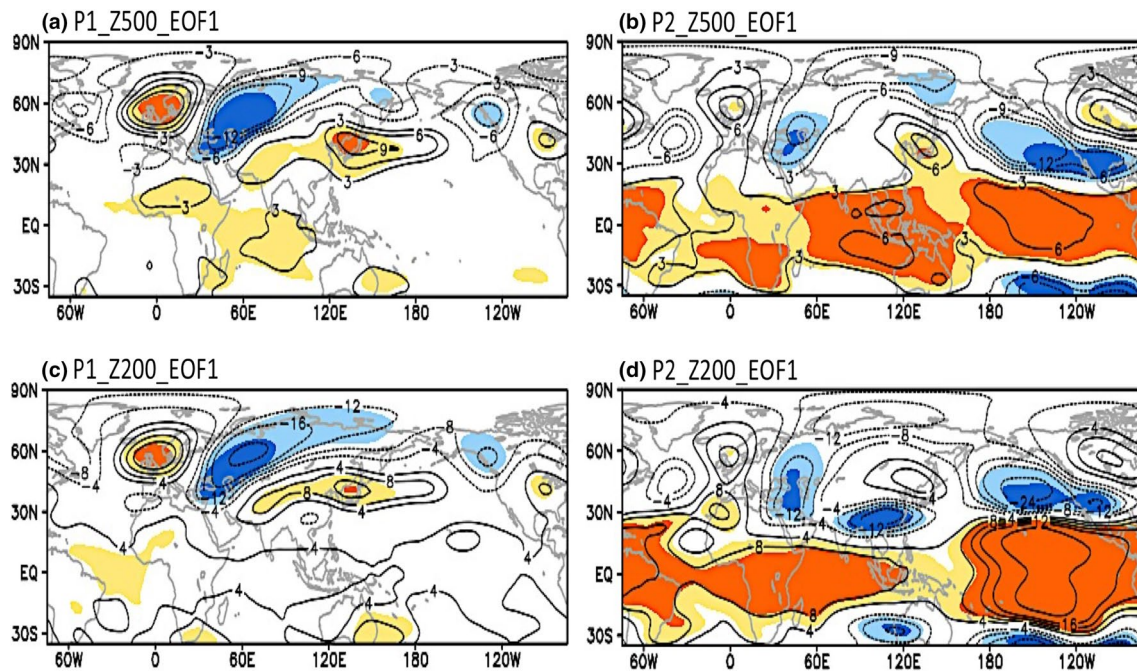


**Fig. 8** The regression maps of **a, b** geopotential height at 500-hPa and **c, d** geopotential height at 200-hPa onto the PC1 time series associated with EOF-1 for P1 [1950/51–1983/84] (**a, c**) and P2 [1984/85–2014/15] (**b, d**). Solid (dashed) contours denote positive

(negative) values and zero lines are omitted. The contour interval is 3 m in **a, b**; and 4 m in **c, d**. The light and dark shadings in the figures (**a–d**) indicate that the correlation coefficients are significant at  $p < 0.10$  and  $p < 0.01$ , respectively

anomalies associated with EOF-1 for P1 (Fig. 8a, c) are analogous to those of SLP, dominated by a zonally oriented wave train-like pattern covering the entire extratropical Northern Hemisphere. Here, the most prominent features are the two dominant positive centres of action located over Western Europe and the mid-latitude Asian sector accompanied by an anomalously strong negative anomaly centre over western Russia, north of the Caspian Sea. This stationary wave structure of large-amplitude ridges and troughs is quasi-barotropic (Figs. 7c, 8a, c) and seems a reminiscent of the positive phase of the EA–WR teleconnection (Liu et al. 2014; Lim and Kim 2016; Gao et al. 2016) or the type 2 Eurasian pattern described in Barnston and Livezey (1987). This result shows that in P1, EOF-1 variability is more closely related to the Northern Hemisphere extratropical teleconnections rather than to tropical forcings.

In P2, the atmospheric circulation anomalies that are related to EOF-1 are notably different in structure and source from that of P1. Pronounced positive height anomalies dominate the tropics in P2, accompanied by a Rossby wave train that emanates from the tropics to the extratropics in response to the El Niño-related forcing and produces both eastward- and westward-propagating stationary waves in the upper troposphere as described in Shaman and Tziperman (2016). An important feature apparent in the 500-hPa (Fig. 8b) and 200-hPa (Fig. 8d) regressed height anomalies is that in addition to the extratropical barotropic wave response induced by the ENSO-related diabatic heating; two westward-propagating baroclinic waves, symmetric about the equator in both hemispheres, are much clearer and stronger in the recent P2 period than for the full-period relationship observed in Fig. 3. A further comparison of the atmospheric circulation anomalies in Fig. 8 with those in Fig. 3 suggest that in the full-period analysis (i.e., Fig. 3) much of the strength of the barotropic signal appears to come from the early P1 period when CSWA precipitation is not related to ENSO.

In a recent study on central Asia, Yin et al. (2014) indicated that both EA–WR and ENSO are related to the regional wintertime precipitation variability through changes in the winter westerly circulation flow and intensity. These changes can be seen clearly in the regressed zonal and meridional wind component anomalies obtained at 200-hPa for P1 and P2 in Fig. 9. In P1, associated with the positive EA–WR phase noted in height anomalies, a westerly zonal anomaly flow appears over the CSWA region between 25°N and 45°N latitude (Fig. 9a). Correspondingly, a large-scale wave train-like pattern can be seen embedded in the regressed meridional wind for P1 (Fig. 9c) with maximum amplitude waves over the high latitude North Atlantic, Europe, and western Russia, with the structure quite similar to the EA/WR wave pattern observed in Fig. 1d of Lim and Kim (2016). Here the combined effect of the upper-tropospheric zonal and meridional wind anomalies over CSWA creates an anomalous

large-scale anticyclone-cyclone couplet at the surface (700-hPa, Fig. 9e). This couplet exerts a strong meridional flow to the west of the CSWA region, accompanied by a weaker zonal flow to the south that appears to be coming from the Atlantic Ocean along the path across North Africa to CSWA between 25°N and 30°N latitude. The prevailing conditions result in a stronger surface cyclonic activity and an enhanced southwesterly flow over the CSWA region, bringing moisture from the Arabian Sea to as far as the Atlantic. On the other hand in P2, the El Niño-related upper-tropospheric zonal wind circulation anomalies over CSWA are associated with the intensification and equatorward shift of the subtropical westerly jet stream (Fig. 9b) and a conspicuous wave-like structure over the Atlantic–European sector in the meridional wind anomalies (Fig. 9d). This pattern favours enhanced southwesterly winds and moisture advection into CSWA from the Arabian Sea and tropical Africa (Fig. 9f).

The results shown here indicate that the leading EOF mode of CSWA winter precipitation is associated with notably different circulation structures and sources of variability in P1 and P2. However, general characteristics of the large-scale circulation anomalies associated with EOF-1 in P2 share many similarities with those obtained for the full analysis period (1950/51–2014/15; Fig. 3) discussed in Sect. 4.1. A closer inspection, however, reveals some notable differences between the two periods most of which are confined locally over mid-latitude Eurasia. For example, the EOF-1 associated atmospheric circulation anomalies in the regressed SLP and geopotential height fields are more pronounced and significant at the 99% confidence level over the European mainland and CSWA region in the period 1950/51–2014/15 (Fig. 3b–d), compared to those in P2. Also, the 200-hPa zonal wind anomalies for (1950/51–2014/15) period in Fig. 3e exhibits a bifurcation of the westerly jet at approximately 30°N–58°E with one branch propagating southward of the CSWA region and the other northeastward over to southern Siberia and then towards north Japan. In P2 (Fig. 9a) no such regional bifurcation is observed in the upper-level zonal wind anomalies, other than the El Niño-related southward displacement of the subtropical jet close to 28°N latitude. Furthermore, the regressed meridional wind anomalies depicted in Fig. 3f displays a wave train pattern dominated by strong (significant at 99% confidence level) anticyclonic-cyclonic regional circulation centres over western Europe–CSWA region, in comparison to those observed in P2 (Fig. 9d).

Our analysis suggests that on the regional scale many of the above-noted spatial differences are a result of the extratropical teleconnection response observed in P1 (i.e. 1950/51–1984/85); that without the ENSO signal, are constrained mainly over the mid-to-high latitudes of the Northern Hemisphere. However, with the significant inter-decadal change of the connection between ENSO and EOF-1 around



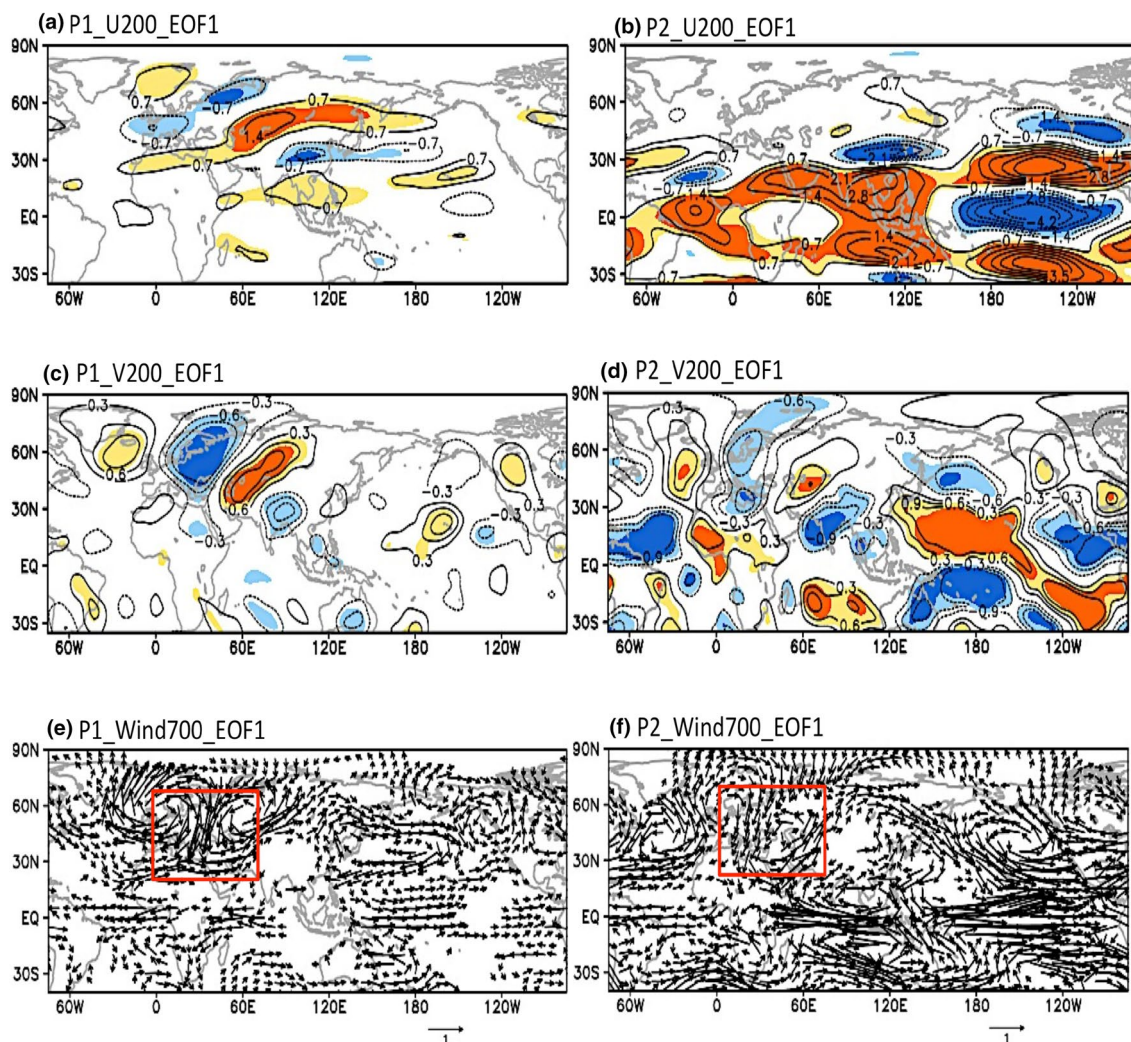


**Fig. 9** The regression maps of **a**, **b** zonal winds at 200-hPa, **c**, **d** meridional winds at 200-hPa, and **e**, **f** wind vectors at 700-hPa onto the PC1 time series associated with EOF-1 for P1 [1950/51–1983/84] (**a**, **c**, **e**) and P2 [1984/85–2014/15] (**b**, **d**, **f**). Solid (dashed) contours

denote positive (negative) values and zero lines are omitted. The contour interval is 0.7 m/s in **a**, **b**; and 0.3 m/s in **c**, **d**. The light and dark shadings in the figures (**a**–**d**) indicate that the correlation coefficients are significant at  $p < 0.10$  and  $p < 0.01$ , respectively

the early 1980s, the strong atmospheric circulation anomalies associated with extratropical processes (e.g. positive EA–WR pattern) in P1 are linearly superimposed by the anomalous atmospheric circulations forced by the warm ENSO conditions throughout the Northern Hemisphere in P2. In fact, the teleconnection pathway or the atmospheric bridge through which the aforementioned modes of climate variability influence the EOF-1 variability in P1 and P2 are quite similar in spatial structure and geographical position over much of Western Europe and Central Asia, as evidenced by the individual stationary barotropic Rossby wave pattern in Fig. 8. This feature likely favours the superposition of the atmospheric circulation anomalies in P2 onto those observed over the mid-to-high latitudes in P1, resulting in a linearly combined atmospheric response which is similar to the one obtained for the full period (1950–51–2014/15) in Fig. 3.

The above results corroborate the findings of Hoell et al. (2014a, b) who showed that the leading mode of CSWA winter precipitation is related to SST anomalies associated with the ENSO phenomenon. However, it has been identified in this study that in addition to ENSO the EA–WR pattern also contributed significantly to the variability of EOF-1; but it is the ENSO's response that appears more pronounced given its significant relationship with EOF-1 in recent years.

## 5.2 The interdecadal change of ENSO-related circulations in P1 and P2

Many of the previous studies have reported that changes in ENSO characteristics since the late 1970s (Wang 1995; Gu and Philander 1997; An and Wang 2000) have affected the variability and predictability of the tropical-extratropical



teleconnections in the Northern Hemisphere, and their associated seasonal climate anomalies (Larkin and Harrison 2005; Jia et al. 2014; Rana et al. 2018; Hoell et al. 2018; Ahmadi et al. 2019). Consistent with the research cited above, our results also demonstrate that the impact of ENSO on CSWA wintertime precipitation climate significantly increased after the mid-1980s. To support these findings, we briefly investigate the changes in ENSO-related circulation anomalies from P1 to P2, for which regression maps of SST, SLP, and Z200 onto Niño-3.4 index are generated and presented in Fig. 10.

Corresponding to a positive Niño 3.4 index, significant positive SST anomalies are observed over the tropical central-eastern Pacific Ocean along and negative SST anomalies in the Western Pacific for both P1 (Fig. 10a) and P2 (Fig. 10b). Here the most notable difference in the ENSO-related SST anomalies is the increase in the strength of the tropical and extratropical Pacific SST anomalies in P2, with a sharp gradient in equatorial SST anomalies between the western and central Pacific Ocean. These results suggest

that the enhanced SST anomaly contrast in the west Pacific Ocean, due to the increased warming in the western Pacific sector since the mid-1980s (as seen in Fig. 10b) has contributed to the changes in the strength of ENSO teleconnections both globally and over southwest Asia (e.g., Barlow et al. 2002; Hoell and Funk 2013; Hoell et al. 2014a, b).

Consistent with the SST anomaly spatial structure, the regression maps of SLP onto Niño-3.4 index for P1 (Fig. 10c) and P2 (Fig. 10d) resemble the Southern Oscillation pattern in the tropics, with significant anomalous negative SLP anomalies over the North Pacific Ocean for both the periods. Although similar in spatial distribution, the magnitude of SLP anomalies in P2 are comparatively stronger to those in P1, suggesting a closer relationship between the tropical Pacific SST variability and the North Pacific atmospheric circulations in recent decades as reported in Jo et al. (2015) and Yeh et al. (2015). Additionally, the regression maps generated for the 200-hPa geopotential height fields display quite different height anomaly patterns over the Northern Hemisphere in P1 (Fig. 10e) and P2 (Fig. 10f). As

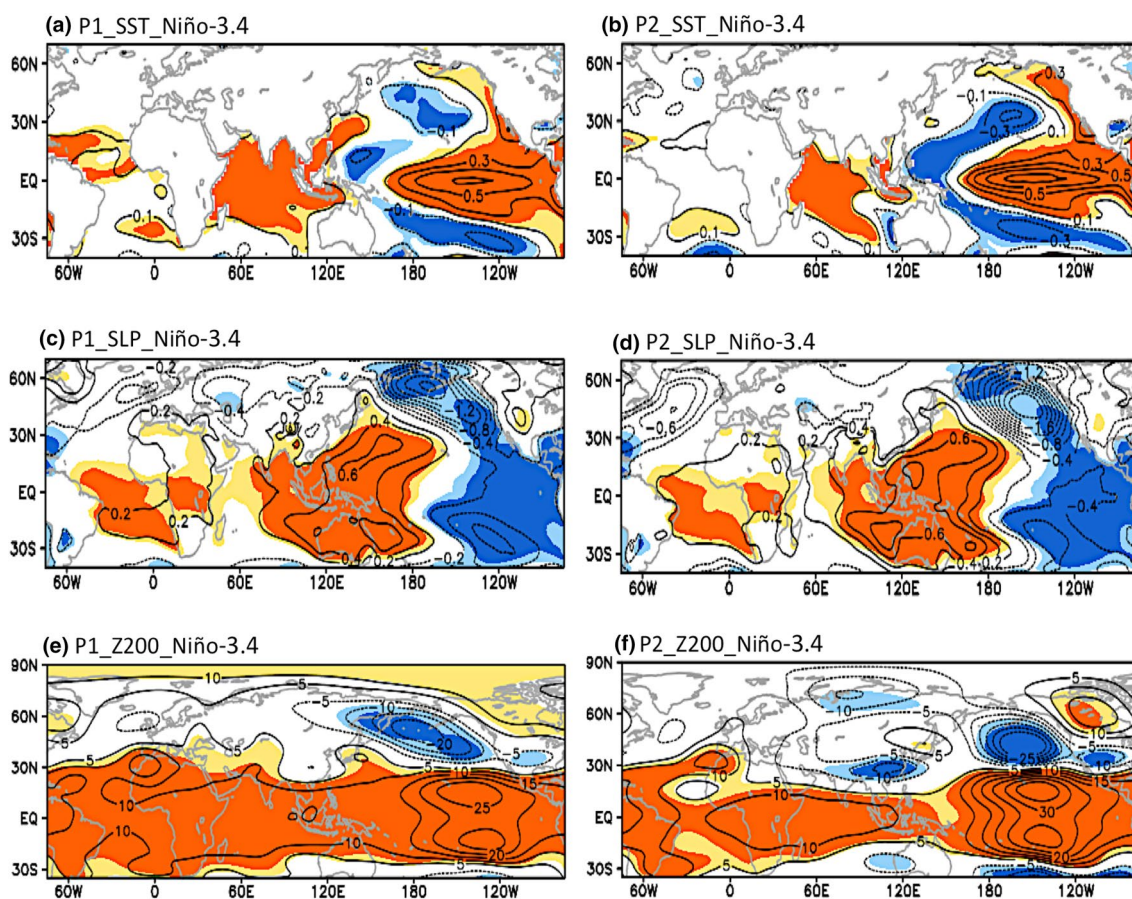


**Fig. 10** The regression maps of **a, b** SST, **c, d** SLP and **e, f** geopotential height at 200-hPa onto Niño-3.4 index for P1 [1950/51–1983/84] (**a, c, e**) and P2 [1984/85–2014/15] (**b, d, f**). Solid (dashed) contours denote positive (negative) values and zero lines are omitted. The con-

tour interval is 0.1 °C in **a, b**; 0.2 hPa in **c, d**; and 5 m in **e, f**. The light and dark shadings in the figures (**a–f**) indicate that the correlation coefficients are significant at  $p < 0.10$  and  $p < 0.01$ , respectively

evidenced by the statistically significant circulation anomalies in the mid-to-high latitudes of Asia, it is apparent that the strength of ENSO-induced atmospheric teleconnection increased substantially in P2. It is also worth noting that the ENSO-related atmospheric circulation anomalies in P2 (Fig. 10f) are fairly similar to those obtained for EOF-1 in P2 (Fig. 8b, d), implying that in this period CSWA precipitation variability was strongly linked to the atmospheric teleconnection forced by ENSO. On the other hand, a clear difference exists between ENSO-forced (Fig. 10e) and EOF-1 related circulation anomalies (Fig. 8a, b) in P1, suggesting that prior to the mid-1980s CSWA precipitation was likely controlled by the non-ENSO modes.

Based on the findings of the studies cited above and the results obtained here, it can be suggested that the possible mechanism that influenced the interdecadal changes of the relationship between ENSO and CSWA wintertime precipitation after the mid-1980s was related to the increased warming in the tropical western Pacific relative to the central Pacific Ocean.

## 6 Summary and discussion

In this study, we analyzed the spatial–temporal variability of the leading three modes of CSWA winter precipitation for the period 1950/51–2014/15. We also investigated the relationship of these modes with the large-scale atmospheric circulations and the global SST. Results show that the first mode (Fig. 2a) is characterized by a spatially coherent mono-sign structure over the entire domain. It represents the year-to-year variability of CSWA winter precipitation that includes a strong contribution of ENSO. The PC1 time-series is significantly correlated at the 99% confidence level with both the observed wintertime precipitation ( $r=0.93$ ) and the Niño 3.4 index ( $r=0.49$ ). El Niño-related Pacific SST anomalies produce an anomalous low pressure (trough) over CSWA via the equivalent barotropic and baroclinic atmospheric circulation response. These conditions favour a region-wide precipitation-enhancing ascent resulting in an enhanced southwesterly moisture flow from the Arabian Sea and Indian Ocean basin (Fig. 3g) that is responsible for positive precipitation loadings over CSWA.

The second mode (Fig. 2b) displays a meridional dipole structure with opposite variations in precipitation north–south of approximately 35°–37°N latitude, indicating a meridional shift in the position and/or intensity of the subtropical wintertime westerly jet over CSWA. The atmospheric circulation anomalies associated with EOF-2 (Fig. 4) are confined mainly over the mid-to-high latitudes of the Northern Hemisphere. It appears that this mode is influenced by a combination of teleconnection processes including both extratropical and tropical (e.g. NAO, EA–WR, Siberian

High, ENSO, and others) that have been previously linked to the changes in the Northern Hemisphere storm track dynamics (Yin et al. 2014; Cohen et al. 2014; Lioubimtseva 2015) either directly or by way of partially modulating the strength of the concomitant teleconnections (Rana et al. 2018). Our results suggest that among other physical processes, the two underlying mechanisms that likely play a role in modulating the strength of the westerly circulation flow over CSWA is related to the westward extension of the Siberian High and the northwestward nudging of the NPO/WP pattern. While further analyses need to be done in this line, here it can only be hypothesised that the combined response of the two forcings (Fig. 4g) directs the eastward propagating storm systems to a more southerly track, resulting in positive (negative) precipitation loadings on the southern (northern) side of the CSWA region.

The third mode (Fig. 2c) of CSWA winter precipitation is expressed as a west–east dipole pattern across the study region. This mode is possibly related to the longitudinal variations in the mean structure and flow (ridges and troughs) of the subtropical jet stream over CSWA which in turn are closely linked to the magnitude of the meridional temperature/pressure gradient between the equatorial regions and higher latitudes. The most prominent spatial characteristics of the large-scale anomalies associated with EOF-3 are its strong and statistically significant relationship with the tropical Ocean SSTs and a clear midlatitude-tropical link in the atmospheric circulation anomalies (Fig. 5). Another distinct feature in the extratropical Northern Hemisphere is a tripolar structure similar to the type 1 Eurasian pattern or the Scandinavian pattern. It is likely (in agreement with Liu et al. 2014), the observed pattern is related to the significant (99% confidence level) SST anomalies observed in the tropical Indian Ocean (Fig. 5a). The air-sea interaction is through a well-organized wave train located upstream of the Indian Ocean that forms an anomalous anticyclone-cyclone couplet over Europe and the Ural region (Fig. 5g), resulting in regional precipitation changes over the western and eastern flanks of CSWA.

In this study, we also investigated the inter-decadal change of connection between ENSO and the first EOF mode of CSWA winter precipitation for two subperiods, 1950/51–1983/84 (P1) and 1984/85–2014/15 (P2). Using the Niño-3.4 index as an indicator of ENSO, the sliding correlation between PC1 and the wintertime Niño-3.4 index showed that the impact of ENSO on EOF-1 was weak in P1; but strong and statistically significant in P2 (Fig. 6). Notable differences are observed in the climate anomalies associated with EOF-1, before (P1) and after (P2) the 1980s. In P1, the EOF-1 related atmospheric circulation anomalies are confined over the mid-to-high-latitudes of the Northern Hemisphere and are characterized by a large-scale zonally oriented quasi-barotropic Rossby wave structures with distinct centres of action over the

European continent, Western Russia and East Asia, similar to the positive phase of the EA–WR teleconnection (Figs. 7, 8). In P2, significant El Niño–type SST anomalies are observed over the tropical Pacific Ocean with anomalous atmospheric circulations extending throughout the Northern Hemisphere (Fig. 7). The underlying teleconnection mechanisms are fairly similar in spatial structure and impact area to those associated with EOF-1 for the full analysis period (1950/51–1983/84; Fig. 3).

It is a noteworthy finding that even though the large-scale climate anomalies associated with EOF-1 display markedly different characteristics in P1 and P2, the teleconnection pathway through which EA–WR and ENSO impact the regional climate of CSWA are quite similar for both the sub-periods. Based on the results presented herein, it can be suggested that the EOF-1-related atmospheric circulation anomalies that appeared to be forced by El Niño conditions in the full analysis period (1950/51–1983/84) are likely a linear superimposition of atmospheric circulations associated with the extratropical EA–WR pattern in P1 by those associated with El Niño in P2. Detailed identification of the dynamical causes related to the inter-decadal change of connection between ENSO and the first EOF mode of CSWA winter precipitation is beyond the scope of the present study. Nonetheless, to gain insights on the possible mechanisms that may have contributed to this change were briefly examined (Fig. 10). Consistent with the findings of some of the previous studies, our results demonstrated that the strong SST anomaly gradient between the western and the central Pacific Ocean played a significant role in forcing anomalous ENSO-related atmospheric response over the CSWA region.

The study improves our understanding of CSWA's wintertime precipitation climate and its relationships with the large scale global and regional teleconnections. These findings have important implications for CSWA, given that an improved understanding of the impact and role of the dominant forcings can eventually lead to improvements in the seasonal predictive skill of the regional precipitation. However, a closer investigation into the role of Siberian High and the NPO pattern in modulating the atmospheric circulation over CSWA would be desirable to support some of the physical mechanisms proposed in the study.

**Acknowledgements** The authors would like to extend their sincere thanks to the Victoria University of Wellington (VUW), New Zealand for supporting this research. The lead author acknowledges VUW for the Doctoral Scholarship Award.

## References

- Ahmadi M, Salimi S, Hosseini SA, Poorantiyosh H, Bayat A (2019) Iran's precipitation analysis using synoptic modeling of major teleconnection forces (MTF). *Dyn Atmos Oceans* 85:41–56
- An S-I, Wang B (2000) Interdecadal change of the structure of the ENSO mode and its impact on the ENSO frequency. *J Clim* 13:2044–2055
- Barlow M, Hoell A (2015) Drought in the Middle East and Central-Southwest Asia during Winter 2013/14. *Bull Am Meteorol Soc* 96:S71–S76
- Barlow M, Tippett MK (2008) Variability and predictability of central Asia river flows: Antecedent winter precipitation and large-scale teleconnections. *J Hydrometeorol* 9:1334–1349
- Barlow M, Cullen H, Lyon B (2002) Drought in central and southwest Asia: La Niña, the warm pool, and Indian Ocean precipitation. *J Clim* 15:697–700. [https://doi.org/10.1175/1520-0442\(2002\)015<0697:DICASA>2.0.CO;2](https://doi.org/10.1175/1520-0442(2002)015<0697:DICASA>2.0.CO;2)
- Barlow M, Wheeler M, Lyon B, Cullen H (2005) Modulation of daily precipitation over Southwest Asia by the Madden–Julian Oscillation. *Mon Weather Rev* 133:3579–3594. <https://doi.org/10.1175/mwr3026.1>
- Barlow M, Hoell A, Colby F (2007) Examining the wintertime response to tropical convection over the Indian Ocean by modifying convective heating in a full atmospheric model. *Geophys Res Lett* 34:L19702. <https://doi.org/10.1029/2007GL030043>
- Barlow M, Zaitchik B, Paz S, Black E, Evans J, Hoell A (2016) A review of drought in the Middle East and Southwest Asia. *J Clim* 29:8547–8574. <https://doi.org/10.1175/jcli-d-13-00692.1>
- Barnston AG, Livezey RE (1987) Classification, seasonality and persistence of low-frequency atmospheric circulation patterns. *Mon Weather Rev* 115:1083–1126
- Barriopedro D, García-Herrera R, Lupo AR, Hernández E (2006) A climatology of Northern Hemisphere blocking. *J Clim* 19:1042–1063
- Bond N, Overland J, Spillane M, Stabeno P (2003) Recent shifts in the state of the North Pacific. *Geophys Res Lett* 30(23):2183. <https://doi.org/10.1029/2003GL018597>
- Bueh C, Nakamura H (2007) Scandinavian pattern and its climatic impact. *Scandinavian pattern and its climatic impact. Q J R Meteorol Soc* 133:2117–2131. <https://doi.org/10.1002/qj.173>
- Cai WJ et al (2015) ENSO and greenhouse warming. *Nat Clim Change* 5:849–859
- Cannon F, Carvalho LMV, Jones C, Bookhagen B (2014) Multi-annual variations in winter westerly disturbance activity affecting the Himalaya. *Clim Dyn*. <https://doi.org/10.1007/s00382-014-2248-8>
- Cannon F, Carvalho LM, Jones C, Norris J (2016) Winter westerly disturbance dynamics and precipitation in the western Himalaya and Karakoram: a wave-tracking approach. *Theor Appl Climatol* 125:27–44
- Cassou C, Terray L, Hurrell JW, Deser C (2004) North Atlantic winter climate regimes: spatial asymmetry, stationarity with time, and oceanic forcing. *J Clim* 17:1055–1068
- Cheung HN, Zhou W, Mok HY, Wu MC (2012) Relationship between Ural-Siberian blocking and the East Asian winter monsoon in relation to the Arctic Oscillation and the El Niño–Southern Oscillation. *J Clim* 25:4242–4257
- Cohen J et al (2014) Recent Arctic amplification and extreme mid-latitude weather. *Nat Geosci* 7:627–637
- Comas-Bru L, McDermott F (2013) Impacts of the EA and SCA patterns on the European twentieth century NAO–winter climate relationship. *Q J R Meteorol Soc*. <https://doi.org/10.1002/qj.2158>
- Compo GP, Sardeshmukh PD (2010) Removing ENSO-related variations from the climate record. *J Clim* 23:1957–1978
- Di Lorenzo E et al (2008) North Pacific Gyre Oscillation links ocean climate and ecosystem change. *Geophys Res Lett* 35:L08607. <https://doi.org/10.1029/2007GL032838>
- Diaz HF, Hoerling MP, Eischeid JK (2001) ENSO variability, teleconnections and climate change. *Int J Climatol* 21:1845–1862
- Francis JA, Vavrus SJ (2012) Evidence linking Arctic amplification to extreme weather in mid-latitudes. *Geophys Res Lett* 39:L06801. <https://doi.org/10.1029/2012GL051000>



- Furtado JC, Di Lorenzo E, Schneider N, Bond NA (2011) North Pacific decadal variability and climate change in the IPCC AR4 models. *J Clim* 24:3049–3067
- Gao T, Yu J, Paek H (2016) Impacts of four northern-hemisphere teleconnection patterns on atmospheric circulations over Eurasia and the Pacific. *Theor Appl Climatol*. <https://doi.org/10.1007/s00704-016-1801-2>
- Gershunov A, Barnett TP (1998) Interdecadal modulation of ENSO teleconnections. *Bull Am Meteorol Soc* 79:2715–2726
- Gill AE (1980) Some simple solutions for heat-induced tropical circulation. *Q J R Meteorol Soc* 106:447–462
- Graf HF, Zanchettin D (2012) Central Pacific El Niño, the “subtropical bridge”, and Eurasian climate. *J Geophys Res Atmos* 117:D01102
- Gu D, Philander S (1997) Interdecadal climate fluctuations that depend on exchanges between the tropics and extratropics. *Science* 275:805–807
- Harris I, Jones PD, Osborn TJ, Lister DH (2014) Updated high-resolution grids of monthly climatic observations—the CRU TS3. 10 Dataset. *Int J Climatol* 34:623–642
- Hasanean H, Almazroui M, Jones P, Alamoudi A (2013) Siberian high variability and its teleconnections with tropical circulations and surface air temperature over Saudi Arabia. *Clim Dyn* 41:2003–2018
- Hassanzadeh P, Kuang Z, Farrell BF (2014) Responses of midlatitude blocks and wave amplitude to changes in the meridional temperature gradient in an idealized dry GCM. *Geophys Res Lett* 41:5223–5232
- Hoell A, Funk C (2013) The ENSO-related west Pacific sea surface temperature gradient. *J Clim* 26:9545–9562
- Hoell A, Funk C (2014) Indo-Pacific sea surface temperature influences on failed consecutive rainy seasons over eastern Africa. *Clim Dyn* 43:1645–1660
- Hoell A, Barlow M, Saini R (2012) The leading pattern of intraseasonal and interannual Indian Ocean precipitation variability and its relationship with Asian circulation during the Boreal Cold Season. *J Clim* 25:7509–7526. <https://doi.org/10.1175/jcli-d-11-00572.1>
- Hoell A, Barlow M, Saini R (2013) Intraseasonal and seasonal-to-interannual Indian Ocean convection and hemispheric teleconnections. *J Clim* 26:8850–8867. <https://doi.org/10.1175/jcli-d-12-00306.1>
- Hoell A, Funk C, Barlow M (2014a) La Niña diversity and northwest Indian Ocean rim teleconnections. *Clim Dyn* 43:2707–2724
- Hoell A, Funk C, Barlow M (2014b) The regional forcing of Northern hemisphere drought during recent warm tropical west Pacific Ocean La Niña events. *Clim Dyn* 42:3289–3311
- Hoell A, Funk C, Magadzire T, Zinke J, Husak G (2015a) El Niño–Southern Oscillation diversity and southern Africa teleconnections during austral summer. *Clim Dyn* 45:1583–1599
- Hoell A, Shukla S, Barlow M, Cannon F, Kelley C, Funk C (2015b) The forcing of monthly precipitation variability over Southwest Asia during the Boreal Cold Season. *J Clim* 28:7038–7056
- Hoell A, Barlow M, Cannon F, Xu T (2017) Oceanic origins of historical Southwest Asia precipitation during the boreal cold season. *J Clim* 30:2885–2903
- Hoell A, Barlow M, Xu T, Zhang T (2018) Cold Season Southwest Asia precipitation sensitivity to El Niño–Southern Oscillation events. *J Clim* 31:4463–4482
- Hoerling M, Kumar A (2003) The perfect ocean for drought. *Science* 299:691–694
- Hoerling MP, Hurrell JW, Xu T (2001) Tropical origins for recent North Atlantic climate change. *Science* 292:90–92
- Huang B et al (2017) Extended reconstructed sea surface temperature, version 5 (ERSSTv5): upgrades, validations, and intercomparisons. *J Clim* 30:8179–8205
- Jia X, Ge J (2017) Interdecadal changes in the relationship between ENSO, EAWM, and the wintertime precipitation over China at the end of the twentieth century. *J Clim* 30(6):1923–1937
- Jia X, Lee J-Y, Lin H, Hendon H, Ha K (2014) Interdecadal change in the Northern Hemisphere seasonal climate prediction skill: part II. Predictability and prediction skill. *Clim Dyn* 43:1611–1630
- Jo H-S, Yeh S-W, Lee S-K (2015) Changes in the relationship in the SST variability between the tropical Pacific and the North Pacific across the 1998/99 regime shift. *Geophys Res Lett* 42:7171–7178
- Kar SC, Rana S (2014) Interannual variability of winter precipitation over northwest India and adjoining region: impact of global forcings. *Theor Appl Climatol* 116:609–623
- Krishnamurti TN (1961) The subtropical jet stream of winter. *J Meteorol* 18:172–191
- Kumar KK, Rajagopalan B, Cane MA (1999) On the weakening relationship between the Indian monsoon and ENSO. *Science* 284:2156–2159
- Larkin NK, Harrison D (2005) Global seasonal temperature and precipitation anomalies during El Niño autumn and winter. *Geophys Res Lett* 32:L16705. <https://doi.org/10.1029/2005GL022860>
- Latif M, Barnett TP (1995) Interactions of the tropical oceans. *J Clim* 8:952–964
- Lim Y-K, Kim H-D (2016) Comparison of the impact of the Arctic Oscillation and Eurasian teleconnection on interannual variation in East Asian winter temperatures and monsoon. *Theor Appl Climatol* 124:267–279
- Linkin ME, Nigam S (2008) The North Pacific Oscillation–west Pacific teleconnection pattern: mature-phase structure and winter impacts. *J Clim* 21:1979–1997
- Lioubimtseva E (2015) A multi-scale assessment of human vulnerability to climate change in the Aral Sea Basin. *Environ Earth Sci* 73:719–729
- Liu Y, Wang L, Zhou W, Chen W (2014) Three Eurasian teleconnection patterns: spatial structures, temporal variability, and associated winter climate anomalies. *Clim Dyn* 42:2817–2839
- Liu H, Liu X, Dong B (2017) Intraseasonal variability of winter precipitation over central Asia and the western Tibetan plateau from 1979 to 2013 and its relationship with the North Atlantic Oscillation. *Dyn Atmos Oceans* 79:31–42
- Lopez-Parages J, Rodriguez-Fonseca B (2012) Multidecadal modulation of El Niño influence on the Euro-Mediterranean rainfall. *Geophys Res Lett* 39:L02704. <https://doi.org/10.1029/2011GL050049>
- Luo D, Lupo AR, Wan H (2007) Dynamics of eddy-driven low-frequency dipole modes. Part I: a simple model of North Atlantic Oscillations. *J Atmos Sci* 64:3–28
- Makorgiannis T, Giles B, Flocas A (1981) The problem of the extension of the Siberian Anticyclone towards southeast Europe, and its relation to atmospheric circulation anomalies over the Northern Hemisphere. *Arch Meteorol Geophys Bioclimatol Ser A* 30:185–196
- Mariotti A (2007) How ENSO impacts precipitation in southwest central Asia. *Geophys Res Lett* 34(16):L16706. <https://doi.org/10.1029/2007GL030078>
- Matsuno T (1966) Quasi-geostrophic motions in the equatorial area. *J Meteorol Soc Japan* 44:25–42
- McGregor S, Timmermann A, Stuecker MF, England MH, Merrifield M, Jin F-F, Chikamoto Y (2014) Recent Walker circulation strengthening and Pacific cooling amplified by Atlantic warming. *Nat Clim Change* 4:888. <https://doi.org/10.1038/nclimate2330>
- Moore G, Renfrew I (2012) Cold European winters: interplay between the NAO and the East Atlantic mode. *Atmos Sci Lett* 13:1–8
- Neelin JD, Battisti DS, Hirst AC, Jin FF, Wakata Y, Yamagata T, Zebiak SE (1998) ENSO theory. *J Geophys Res Oceans* 103:14261–14290
- Oki T, Kanae S (2006) Global hydrological cycles and world water resources. *Science* 313:1068–1072

- Panagiotopoulos F, Shahgedanova M, Hannachi A, Stephenson DB (2005) Observed trends and teleconnections of the Siberian high: a recently declining center of action. *J Clim* 18:1411–1422
- Rana S, McGregor J, Renwick J (2015) Precipitation seasonality over the Indian subcontinent: an evaluation of gauge, reanalyses, and satellite retrievals. *J Hydrometeor* 16:631–651. <https://doi.org/10.1175/JHM-D-14-0106.1>
- Rana S, McGregor J, Renwick J (2017) Wintertime precipitation climatology and ENSO sensitivity over central southwest Asia. *Int J Climatol* 37:1494–1509. <https://doi.org/10.1002/joc.4793>
- Rana S, Renwick J, McGregor J, Singh A (2018) Seasonal prediction of winter precipitation anomalies over Central Southwest Asia: a canonical correlation analysis approach. *J Clim* 31:727–741. <https://doi.org/10.1175/JCLI-D-17-0131.1>
- Rogers JC (1997) North Atlantic storm track variability and its association to the North Atlantic Oscillation and climate variability of northern Europe. *J Clim* 10:1635–1647
- Schär C, Vasilina L, Pertziger F, Dirren S (2004) Seasonal runoff forecasting using precipitation from meteorological data assimilation systems. *J Hydrometeor* 5:959–973
- Schneider U, Becker A, Finger P, Meyer-Christoffer A, Ziese M, Rudolf B (2014) GPCC's new land surface precipitation climatology based on quality-controlled in situ data and its role in quantifying the global water cycle. *Theor Appl Climatol* 115:15–40
- Shabbar A, Huang J, Higuchi K (2001) The relationship between the wintertime North Atlantic Oscillation and blocking episodes in the North Atlantic. *Int J Climatol* 21:355–369
- Shaman J, Tziperman E (2005) The effect of ENSO on Tibetan Plateau snow depth: a stationary wave teleconnection mechanism and implications for the South Asian monsoons. *J Clim* 18:2067–2079
- Shaman J, Tziperman E (2016) The superposition of Eastward and Westward Rossby waves in response to localized forcing. *J Clim* 29:7547–7557
- Sterl A, Van Oldenborgh GJ, Hazeleger W, Burgers G (2007) On the robustness of ENSO teleconnections. *Clim Dyn* 29(5):469–485. <https://doi.org/10.1007/s00382-007-0251-z>
- Stevenson SL (2012) Significant changes to ENSO strength and impacts in the twenty-first century: results from CMIP5. *Geophys Res Lett* 39:L17703. <https://doi.org/10.1029/2012GL052759>
- Strong C, Davis RE (2007) Winter jet stream trends over the Northern Hemisphere. *Q J R Meteorol Soc* 133:2109–2115. <https://doi.org/10.1002/qj.171>
- Van Oldenborgh GJ, Burgers G (2005) Searching for decadal variations in ENSO precipitation teleconnections. *Geophys Res Lett* 32:L15701. <https://doi.org/10.1029/2005GL023110>
- Walker GT, Bliss EW (1932) World weather V. *Mem R Meteorol Soc* 4:53–84
- Wang B (1995) Interdecadal changes in El Niño onset in the last four decades. *J Clim* 8:267–285
- Wilks DS (2006) Statistical methods in the atmospheric sciences (International Geophysics Series; V. 91). Academic Press
- Wolff C, Plessen B, Dudashvili AS, Breitenbach SF, Cheng H, Edwards LR, Strecker MR (2017) Precipitation evolution of Central Asia during the last 5000 years. *Holocene* 27:142–154
- Woollings T, Hannachi A, Hoskins B (2010) Variability of the North Atlantic eddy-driven jet stream. *Q J R Meteorol Soc* 136:856–868
- Yeh SW, Wang X, Wang CZ, Dewitte B (2015) On the relationship between the North Pacific climate variability and the central Pacific El Niño. *J Clim* 28:663–677
- Yin Z-Y, Wang H, Liu X (2014) A comparative study on precipitation climatology and interannual variability in the Lower Midlatitude East Asia and Central Asia. *J Clim* 27:7830–7848. <https://doi.org/10.1175/jcli-d-14-00052.1>

**Publisher's Note** Springer Nature remains neutral with regard to jurisdictional claims in published maps and institutional affiliations.